Numerical optimization of S-shaped intake performance using special cross-sectional profiles

S.H. Sadatpour, A. Madadi[*], and R. Ahadian

Amirkabir University of Technology, *Tehran, Iran*

E-mail: h.sadatpoor@aut.ac.ir; [*]ali.madadi@aut.ac.ir; r.ahadian@aut.ac.ir

An intake has to provide air for the engine uniformly with minimum total pressure loss. Nowadays, regarding the usage of S-shaped intakes, optimization of these ducts has been considered. Uniform distribution of flow at the compressor inlet directly influences the engine performance, and non-uniformity of flow increases surge occurrence possibility. Flow separation along the duct causes a reduction of pressure recovery and engine thrust force. This research has optimized an S-shaped intake to reduce the total pressure loss and flow distortion. The genetic algorithm and artificial neural networks have been combined to decrease the computational cost. Two optimizations, using different conditions, have been studied. In the first case, by modifying centerline coordinates and area ratio of sections, new geometries have been produced, which has caused an improvement of 32.5 % in pressure recovery coefficient and a decrease of 35.8% in flow distortion. In the second optimization, the shape of each section has also been changed. Superellipse, egg-shaped and circular profiles are considered as cross-sections of the duct. The second optimization has improved the pressure recovery coefficient by 35.5 % and decreased flow distortion by 39.2 %.

Keywords: S-shaped intake, genetic algorithm, artificial neural network, flow uniformity, pressure recovery.

Introduction

Intake is a part of a plane whose duty is to provide air for the engine steadily and with minimum total pressure loss. Intakes, despite their simple appearance, are complex parts and should meet many requirements, and if they do not work correctly, the engine performance will be significantly affected.

To reach the maximum thrust under all flight conditions, pressure recovery inside the intake and drag coefficient caused by an external flow should be optimized. One of the essential reasons for pressure recovery reduction is friction and distortion in flow patterns. In a high-velocity flow, boundary layer thickness increases along the duct. The thick boundary layer is sensitive to adverse pressure gradient and can be easily separated. Boundary layer separation causes vortex flows, pressure recovery reduction, and an increase in flow distortion, which increases the possibility of the compressor surge.

Due to the adverse pressure gradient at the end of the upper wall of the S-shaped intake, flow separation is unavoidable in this area. If the cross-sectional planes are designed in such a way that velocity increases at the end of the upper wall and decreases at the end of the lower

wall, the pressure difference between the upper and lower wall in a cross-sectional plane decreases. Hence, the flow separation can be reduced without a change in flow average velocity, which can be achieved by replacing the ellipse profile with the egg-shaped profile in the location of flow separation [1].

Numerous studies have been done to reach better flow field characteristics to reduce flow distortion and improve duct performance. The first projects were based on experimental researches. However, progress in computational systems permits to simulate flow with mathematical models that facilitate S-shaped intake studies.

Most of the experimental research on S-shaped intakes was done by the authors of [2] in 1992. They tested compressible flow inside the S-shaped duct at NASA's Lewis Research Center and presented numerous data about aerodynamic parameters and flow separation mechanisms. This test demonstrated flow field complexity clearly; at the first bend, a significant separation region occurs, which causes a vortex on the symmetry plane and two counter-rotating vortices on the engine face. These secondary flows result in total pressure loss. Besides, it was noted that the flow is still symmetric and severely separates the boundary layer from duct walls.

Numerical simulation of the S-duct has been developing rapidly in recent years. In the work [3], a modified k-ω turbulence model was applied to investigate transonic flow features of an S-duct. The Reynolds stress model was adopted in [4] to analyze the flow field structure of a dual S-duct. The sensitivity of different turbulence models was investigated for the S-duct in the work [5], and the minimal number of grid points yielding an accurate numerical solution is obtained. It was indicated that the result of Menter's k-ω Shear Stress Transport (SST) model was more reliable than the other three models. The authors of [6] simulated the flow field with the FLUENT solver and four turbulence models and deduced that k-ω SST model is better in pressure recovery prediction along the centerline. Computational results are compared with experimental data and demonstrate notable improvement by the lag model for flows with strong shock–boundary-layer interactions.

Another important project was done at Cranfield University in [7]. This project is about unsteady analysis of S-shaped intake with different grids; this research particularly states how medium grids provide results similar to a fine grid, and there is not much difference between the half duct and full duct simulations.

In recent years, optimization processes have been applied to improve the performance characteristics of S-shaped intakes. In addition, these processes improve geometry using design parameters. Some of these researches are summarized here.

The optimum shape of a two-dimensional symmetric diffuser has been optimized for handling incompressible turbulent flow in research [8]. The indigenously developed algorithm uses the CFD software: the FLUENT solver for the hydrodynamic analysis and employs a genetic algorithm (GA) for optimization. The CFD software and the GA have been combined in a monolithic platform for a fully automated operation using some special control commands.

The flow in a rectangular section was investigated in the work [9]. The purpose of the optimization was to maximize C_p and minimize the $DC60$ parameter. The first one is the area-averaged total pressure coefficient, and the second is the distortion coefficient at the exiting plane. The optimized geometry improved C_p and $DC60$ by 58 % and 54 %, respectively.

The work [10] was devoted to the optimization of an S-shaped duct. The flow field has been simulated using the FLUENT solver and turbulence model k-ω SST model. Three geometries have been analyzed: a geometry with the best pressure recovery, the best swirl angle, and a compromise between them. Numerical simulation methods have studied more than 600 geometries.

The efficiency of the duct has been improved through two functions of pressure recovery and swirl angle. The analysis resulted in a 19 % increase in pressure recovery coefficient and a 13 % decrease in distortion swirl.

A fast multi-objective optimization method for S-duct scoop inlets considering both inflow and outflow was developed and validated by the authors of [11]. They developed an automated optimization system integrating the computational fluid dynamics analysis, non-uniform rational B-spline geometric representation technique, and non-dominated sorting genetic algorithm to minimize the total pressure loss and distortion at the diffuser exit. By analyzing the results of a suggested optimal inlet chosen from the obtained Pareto front, total pressure recovery has increased from 97 % to 97.4 %, and total pressure distortion $DC60$ has decreased by 0.0477 (21.7 % of the origin).

In the work [12] the S-shaped ducts were researched using the ball-spine inverse design method. In this method, walls were considered a set of virtual balls that could move freely in a straight direction called the spine. Target pressure distribution along the upper and lower lines is determined so that separation does not occur. The results illustrate that the designed S-shaped duct of this method has a better performance compared to the primary model.

In the work [13] the authors, using Free Form Deformation, optimized an S-shaped duct. The objective of this optimization was to minimize total pressure loss and distortion. A multi-objective genetic algorithm has been used for optimization. The analysis has resulted in a 20 % improvement in total pressure loss and a 10 % reduction in flow distortion.

The authors of [14] has researched the design of an optimized S-shaped duct, considering energy loss and uniformity of outlet flow. The baseline duct is an axisymmetric two-dimensional geometry. Finally, the total pressure loss and normalized outlet radial velocity was improved by 15.6 % and 34.2 %, respectively.

The authors of the work [15] improved a three-dimensional S-shaped aerodynamic performance using a multi-objective optimization strategy. Compared with the main design, the flow distortion coefficient in the optimized duct decreased by 16.3 %, and the total pressure recovery coefficient increased by 1.1 %.

The authors of [16] have optimized a three-dimensional S-shaped duct to reduce the total pressure loss reduction and uniformity improvement. By decreasing 25 % of duct length, pressure recovery and distortion were improved. The main reason for this improvement was the reduction of wall friction due to shorter duct length.

The performance of the duct has been improved only by changing the radius of sections (which are ellipse) and the centerline coordinate.

A three-dimensional S-shaped duct is optimized in the present research by changing the centerline coordinate, area ratio, and shape of the sections. Considered section shapes are superellipse, egg-shaped, and circular profiles. Furthermore, a genetic algorithm, coupled with artificial neural networks and the CFD solver, reduces the computational cost.

1. Problem definition

To reduce the total pressure loss and improve flow uniformity in the S-shaped duct, shape optimization is used. This process is done by coupling genetic algorithms and neural networks to minimize two objective functions: total pressure loss and distortion. A mathematical model must express total pressure loss and distortion based on geometrical parameters for optimizing the duct shape. However, due to exceeding complexity, no model can explicitly anticipate these two objective functions; therefore, multi-layer neural networks are used to estimate two objective functions. At first, an S-shaped duct with available experimental and numerical results is chosen in this paper, and numerical simulation is validated. Then two optimizations are done with two different conditions.
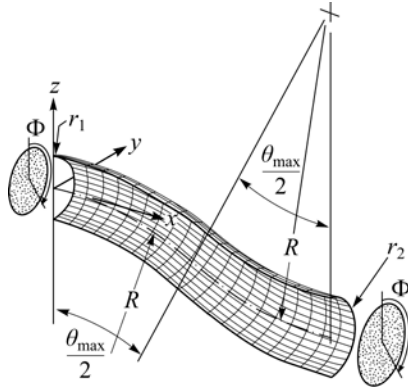
Fig. 1. The initial geometry of the S-shaped duct [2].

1.1. Baseline duct geometry

The initial geometry used is the same as in the work [2] designed in NASA's Lewis Research Center in 1992 (see Fig. 1). Here, the centerline is defined by two circular arcs located in the x-y plane, with a radius of $R = 102.1$ cm and an angle of 30°. The centerline coordinates are obtained from equations (1) to (3) [2].

$$x_{cl} = \begin{cases} R\sin\theta, & 0 \le \theta \le \theta_{max}/2, \\ 2R\sin(\theta_{max}/2) - R\sin(\theta_{max}-\theta), & \theta_{max}/2 \le \theta \le \theta_{max}, \end{cases} \tag{1}$$

$$y_{cl} = \begin{cases} R\cos\theta - R, & 0 \le \theta \le \theta_{max}/2, \\ 2R\cos(\theta_{max}/2) - R(1+\cos(\theta_{max}-\theta)), & \theta_{max}/2 \le \theta \le \theta_{max}, \end{cases} \tag{2}$$

$$z_{cl} = 0. \tag{3}$$

In this geometry, all cross sections of the duct are circular and perpendicular to the center line. The area ratio of the outlet to the inlet is $A_2/A_1 = 1.52$. The duct radius is a function of angle θ shown in equation (4) [2].

$$\frac{r}{r_1} = 1 + 3\left(\frac{r_2}{r_1}-1\right)\left(\frac{\theta}{\theta_{max}}\right)^2 - 2\left(\frac{r_2}{r_1}-1\right)\left(\frac{\theta}{\theta_{max}}\right)^3. \tag{4}$$

Table 1 shows geometrical parameters, and Fig. 2 is presented for better comprehension.

T a b l e 1
Duct geometry parameters

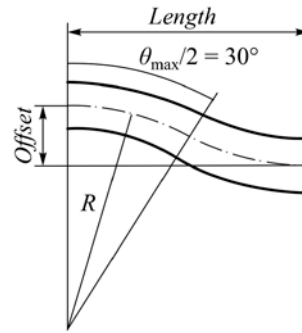| Parameter	Value, cm
R	H
r_1	10.21
r_2	12.57
Offset	27.35
Length	102.1

Fig. 2. Side view of the baseline S-shaped duct.

1.2. Optimization loop

Optimization is done using a genetic algorithm. A genetic algorithm is a well-known innovative and practical algorithm with a wide range of complicated engineering problems.
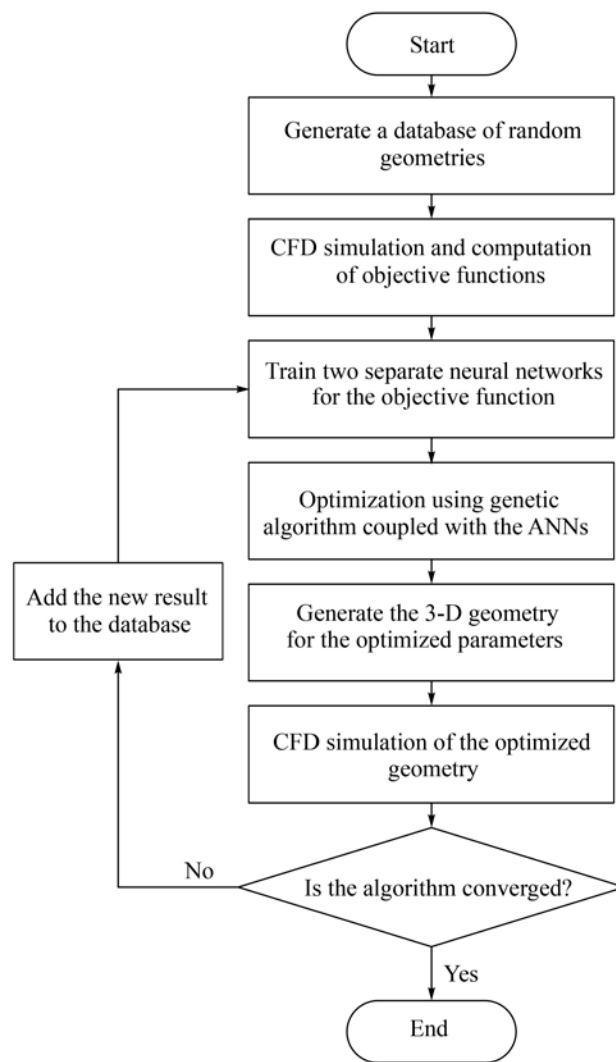
692

Fig. 3. Flowchart of the optimization process.

The optimization procedure is shown in Fig. 3. At the first step, a database containing 40 random geometries is created. The geometries are generated randomly by applying the constraints on the random centerline and shape of the sections. The curvature of the centerline can change only one time, and the width distribution should be increasing from inlet to outlet of the diffuser. The grid is generated, and the flow field is solved for these 40 geometries using CFD solver by finite volume method, and the objective functions are obtained. The neural networks are trained for total pressure loss and flow distortion. The reason for using neural networks is to reduce the computational cost of the optimization procedure. Artificial neural networks (ANN) are used instead of CFD solvers during the optimization procedure. The genetic algorithm optimizes the objective functions predicted by neural networks, and a vector of optimized variables is obtained. Three-dimensional geometry is generated using these variables and then is numerically simulated by the CFD solver. At this step, it is investigated whether it has reached the desired accuracy or not. If the algorithm has not reached the required precision, the numerical calculation results are added to the database. Then, the neural network is trained again, and the loop is continued. Conversely, if it has reached the target accuracy, the optimization procedure is stopped.

T a b l e 2

Details of artificial neural networks

Criteria	Function/value
Number of hidden layers	3
Number of neurons	4
Feeding method	Backpropagation
Number of epochs	200
Convergence goal	10^{-8}
Output function	Linear function
Neuron activation function	Sigmoid
Data division	Random
Training algorithm	Levenberg–Marquardt
Performance	Mean squared error

To achieve the optimal answer, two stopping criteria have been used simultaneously for the genetic algorithm, which are:

1. Generations: is the maximum number of generations produced, which is set equal to 250. It should be noted that the size of the population is 20.

2. Convergence criterion: The algorithm stops if the relative change in the best fitness function value over Stall Generation Limit generations is less than or equal to the function tolerance. The Stall Generation Limit is set to 50 and the Tolerance Function to 10^{-7}. Also, if the difference between the CFD simulation and the ANN is less than 10^{-5}, the optimization procedure is stopped for the outer optimization loop.

It is estimated that neural networks and genetic algorithms reduce the computational cost by 60 % to 80 %. For example, in a similar study [10], which uses only a genetic algorithm, more than 600 different geometries were simulated to achieve the optimal solution. While in this paper, the number of simulations performed to find the optimized geometry is 190.

The neural networks used in this work consist of three hidden layers, each layer containing four neurons. The characteristics of the neural network and the training method are listed in Table 2.

1.3. Objective functions

The flow field in an S-shaped duct is quite complicated and depends on several factors. Therefore, several parameters are used to examine the S-shape duct performance. Among them, the total pressure loss and distortion are chosen as the main objectives here. In this optimization, the same weight factor is considered for each of the objective functions. In other words, the weight factor of each of the objective functions f_1 and f_2 is equal to 0.5.

Total pressure loss

Total pressure loss is due to actual flow behavior and especially flow separation. The pressure recovery coefficient describes this pressure loss, which is calculated using mass flow averaged values.

$$PR = \frac{P_{0,\text{out}}}{P_{0,\text{in}}}, \tag{5}$$

where $P_{0,\text{out}}$ is the mean total pressure at the duct outlet (engine inlet) and $P_{0,\text{in}}$ is total pressure at the duct inlet section. Therefore, the pressure recovery coefficient should reach the highest possible value to reduce pressure loss in the duct. Regarding the fact that optimization methods are designed to minimize objective functions, the objective function should be defined as below:

$$f_1 = 1 - PR. \tag{6}$$

Fig. 4. Definition of 60-degree sectors.

Flow distortion

Distortion is the second objective function; minimizing this parameter improves flow uniformity at the compressor inlet face. Equation (7) is used to calculate the total pressure distortion.

$$f_2 = DC(60) = \frac{P_{0,\text{out}} - P_{0,60}}{q_{\text{out}}}, \qquad (7)$$

here q_{out} is mean dynamic pressure, $P_{0,60}$ is the worst possible pressure in a 60-degree sector at the outlet plane [17]. Figure 4 illustrates the 60-degree sectors in which $DC(60)$ is calculated.
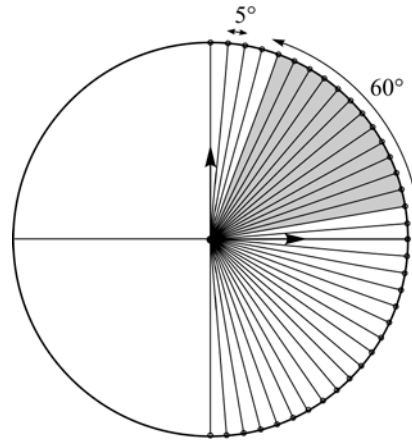
1.4. Geometry parameterization

The first step in an optimization problem is selecting the design variables. In this process, the model is described by several design parameters. In the first optimization, 12 parameters are used to define the duct geometry. Six parameters define the y-coordinates of the S-shape duct central line. Parameters 7 to 12 also define the area ratio of circular sections. All circular sections are assumed perpendicular to the centerline. In Fig. 5, the control points used for generating duct centerline in the first optimization are shown.

In the second optimization, the centerline coordinate and area ratio of the duct sections, the shape of each section are changed. It is better to use superellipse sections instead of ellipse profiles to reduce the occupied space and external drag. Equation (8) is used to generate a super-ellipse section:

$$\frac{y^n}{b^n} + \frac{z^n}{a^n} = 1. \qquad (8)$$

This formula defines a closed curve enclosed in a rectangle of dimensions $2a$ and $2b$. The parameters a and b are called the semi-diameters of the curve. If the value of power n is set to 2, equation (8) becomes a circle relation. As the power n increases, the cross-sectional shape moves away from the circle and approaches the rectangle. This geometry is known as superellipse. Figure 6 shows the super-ellipse geometry for three different values of n.

On the other hand, to accelerate the flow in locations where flow momentum is low, an egg-shaped profile is used to overcome the adverse pressure gradient. Equation (9) is applied to create egg-shaped geometry:

$$\frac{y^2}{b^2} \cdot \frac{1+kz}{1-kz} + \frac{z^2}{a^2} = 1. \qquad (9)$$

The shape of the profile changes by the value of coefficient k. If the coefficient k is set to zero and $a = b$, the egg turns into a circle. Figure 7 shows examples of egg profiles.
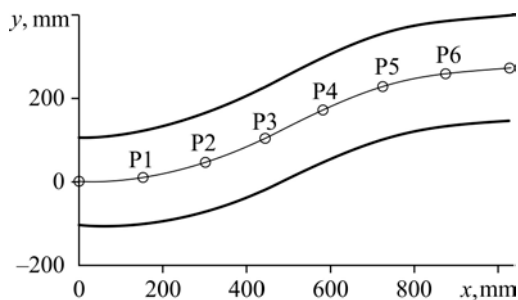

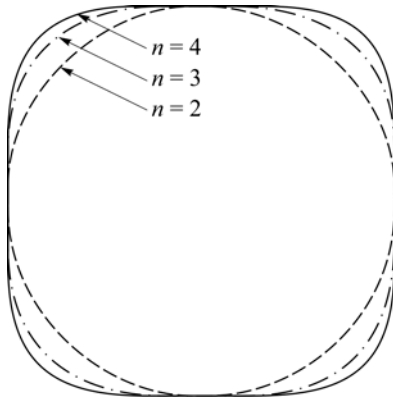*Fig. 5.* Control points used for creating duct centerline in the first optimization
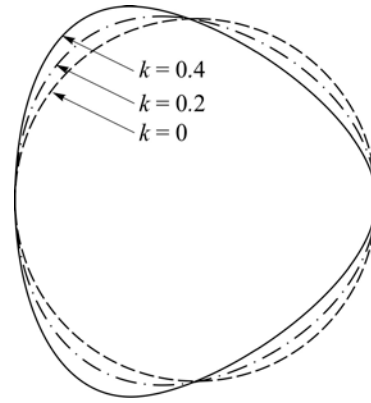
Fig. 6. Superellipse geometry.

Fig. 7. Egg-shape geometry.

An equation is obtained by combining the superellipse and egg-shape profile equation, which contains properties of both profiles.

$$\frac{y^n}{b^n}\frac{1+kz}{1-kz}+\frac{z^n}{a^n}=1. \tag{10}$$

Both equations are changeable to ellipse and circle by specific values of k, n, a, and b. By changing these coefficients smoothly, it is possible to switch from a profile to another one. In this optimization, 18 variables are used to create the duct geometry, four variables are related to the centerline y-coordinate of sections 2–5, 4 variables are related to the area ratio of sections 2–5, and 10 variables are related to section shape determination (k and n in equation (10) for sections 1–5). In Fig. 8, a sample of the S-shaped duct generated by combinatorial sections and 18 parameters is shown.

1.5. Flow field solver

The flow field is simulated using the finite volume CFD solver. In addition, an unstructured grid is used combined with the boundary layer (Fig. 9).

Only half of the duct is modeled to reduce computational cost. Boundary conditions are illustrated in Fig. 9 and Table 3. In the symmetry boundary condition, zero gradients normal to the boundary lead to the reflection of the duct. For the inlet boundary, the values of total pressure and temperature, and flow direction are set. The static pressure is given at the outlet boundary, and other properties are extrapolated from inside the domain. On the wall boundary, the velocity components are set to zero, and the pressure is extrapolated. The adiabatic condition is used for temperature. Based on previous studies [3–6, 10, 11, 14, and 16], the Shear Stress Transport model is used for turbulence effects.
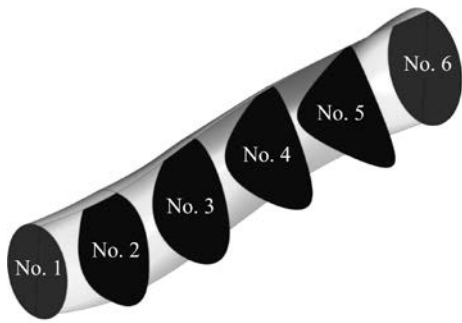

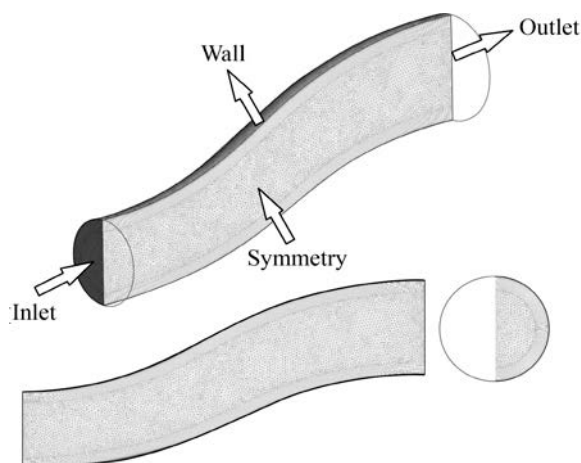Fig. 8. S-shaped duct with combinatorial sections and 18 parameters.

Fig. 9. Perspective view of the generated grid
with boundary conditions.

Table 3
Boundary conditions

Value	Location
Total pressure, $P_{0,in}$ = 129.241 kPa	
Static temperature, T = 268 K	Duct inlet
Mach number, M = 0.6	
Static pressure, P = 117.048 kPa	Duct outlet

2. Results of baseline geometry

Before the optimization procedure, the accuracy and grid independency of the CFD results should be assured. So, at first, the value of y^+ on the walls is investigated, and then grid independency is checked, and in the end, the solver validation is studied.

2.1. Investigation y^+

It is necessary to control the height of the first wall-adjacent cells to illustrate boundary layer behavior. The *k-ω* SST turbulence model is used. The appropriate y^+ for this turbulence model is near to 1. The height of the first boundary layer cell is adjusted so that the y^+ value is in the intended range. For the generated grid, the mean value of y^+ on walls is 0.8. In Fig. 10, the y^+ value is plotted on two lines of 0 and 180 degrees.
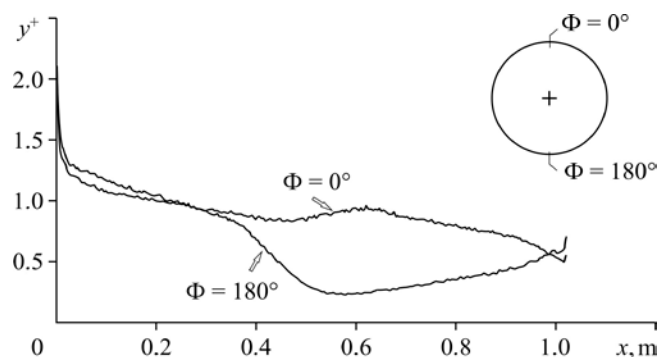

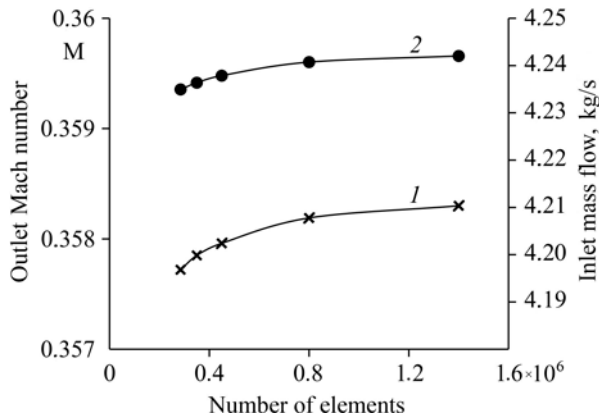*Fig. 10.* The value of y^+ on two lines with angles of 0 and 180°.

Fig. 11. Grid study for duct outlet Mach number (*1*) and inlet mass flow (*2*).

2.2. Grid study

A grid independency process is required to ensure that by changing the grid size, obtained numerical results will not vary by the grid resolution. For example, the inlet mass flow rate and Mach number on the duct outlet plane of five grid sizes are shown in Fig. 11. In Table 4, the difference in performance parameters is compared in various grid sizes with the finest grid.

Comparison of the results of different grids

Duct outlet total pressure, kPa (difference with the finest grid)	Duct outlet Mach number (difference with the finest grid)	Duct inlet mass flow rate, kg/s (difference with the finest grid)	Number of elements
128.099 (0.03 %)	0.3577 (0.16 %)	4.235 (0.17 %)	285 000
128.107 (0.02 %)	0.3578 (0.14 %)	4.236 (0.13 %)	350 000
128.114 (0.01 %)	0.3580 (0.08 %)	4.238 (0.10 %)	450 000
128.099 (0.03 %)	0.3577 (0.16 %)	4.235 (0.17 %)	285 000
128.127 (0.005 %)	0.3582 (0.03 %)	4.241 (0.03 %)	800 000
128.134 (0 %)	0.3583 (0 %)	4.242 (0 %)	1 400 000

Based on the results, it can be concluded that the grid with 800 000 elements can be used for CFD simulations, and the results will not be changed by refining the grid sizes.

2.3. Validation

For validation, numerical analysis results should be compared to existing experimental data. Therefore, the intake introduced by Wellborn [2] is selected as the baseline geometry because the experimental data is available. In Fig. 12, the pressure coefficient along the duct for three peripheral positions of 10°, 90°, and 170° is illustrated.

It should be mentioned that C_p is a dimensionless pressure coefficient which is explained in equation (11):

$$C_p = \frac{P - P_{cl}}{P_{0,cl} - P_{cl}},\qquad(11)$$

P_{cl} and $P_{0,cl}$ are static pressure and total pressure, respectively, at the central point of the inlet plane. If the designer uses high-fidelity methods, the accuracy of the design is improved. However, the computational cost is increased.
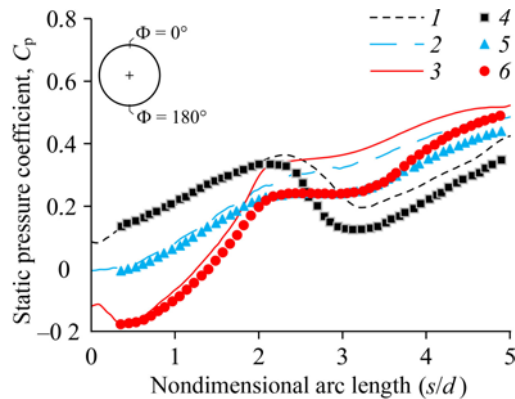

Fig. 12. Comparison of simulation results (*1 – 3*) with experiment data (*4 – 6*) [2] for three angle positions $\varphi = 10°$ (*1, 4*), 90° (*2, 5*), 170° (*3, 6*)

3. Optimization results

Two different optimizations with different conditions are done on Wellborn's geometry [2], explained in the following sections.

3.1. Optimization by changing the area ratio of sections and centerline coordinates

In this optimization, the inlet and outlet of the duct are constant, and only the area ratio of sections and the centerline *y*-coordinate are changed. The number of CFD simulations done to find the optimized geometry is 190. In Table 5, the results of the optimized geometry are compared to the baseline geometry. As is seen, the first objective function, total pressure loss, and the second one, distortion, are improved by 32.5 % and 35.8 %, respectively.

Table 5

Comparison between the results of baseline geometry and the optimized geometry

Objective functions	Baseline geometry	First optimization	Improvement
$f_1 = (1 - PR)$	0.87 %	0.59 %	32.5 %
$f_2 = DC(60)$	0.107	0.0685	35.8 %

Figure 13 shows the velocity contours in the symmetry plane of the duct in the optimized and baseline geometries. As seen in the first optimization geometry, the flow separation region after the first bend is eliminated remarkably, which results in lower total pressure loss and flow distortion at the engine inlet. The optimized geometry has a severe increase in area in the first part of the duct, and after that, the area remains almost constant. These changes bring along a reduction of total pressure loss and more uniformity of flow.
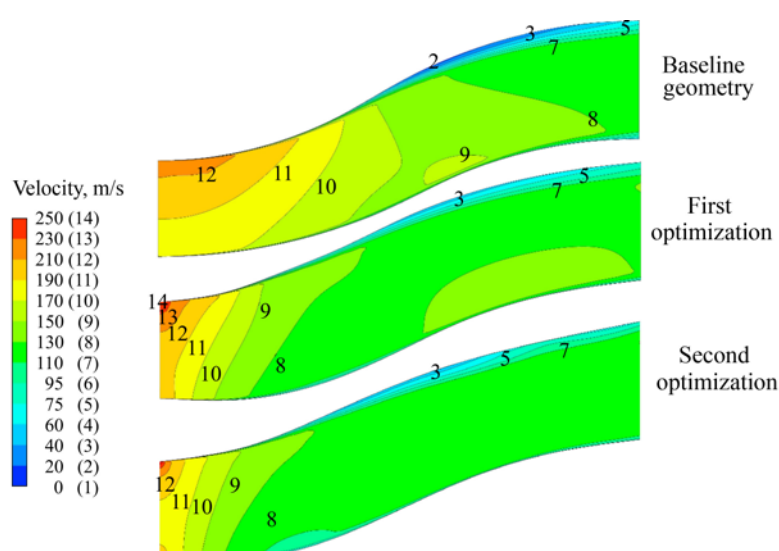

Fig. 13. Comparison of velocity magnitude contours on the symmetry plane in the baseline geometry and the optimized geometries.

Fig. 14. The boundaries of the upper and lower lines of the duct on the symmetry plane.

1 — baseline geometry, *2* — first optimization, *3* — second optimization.

Figure 14 illustrates the boundaries of the upper and lower duct lines on the symmetry plane for better comparison between optimized and baseline geometries.

Figure 15 shows the total pressure loss contours at the duct outlet plane in optimized and baseline geometries. As illustrated in the first optimization, the thickness of the layer with low momentum is reduced, and flow uniformity is improved.

Figure 16 shows streamlines in the optimized geometry. As it could be seen, flow passes the duct path smoothly and leaves the duct without any separation or vortexes.

3.2. Optimization by changing the section shapes

In the second optimization, in addition to the centerline *y*-coordinates and area ratio of sections, the shape of each section is changed. The section shapes are circular, superellipse, and egg-shaped. The main reason for using ducts with various section profiles is to accelerate the flow in locations where flow momentum is low to overcome adverse pressure gradient and prevent flow separation. Table 6 shows the optimization results summary. As is seen, total pressure loss and distortion are improved by 35.7 % and 39.2 %, respectively.

Table 6

Comparison between the results of baseline geometry and the second optimized geometry

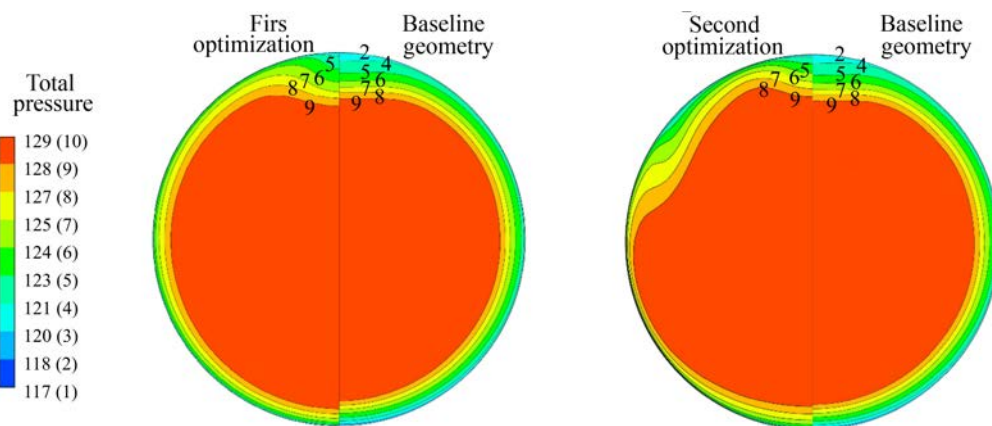| Objective function	Baseline geometry	Second optimization	Improvement
$f_1 = (1 - PR)$	0.87 %	0.56 %	35.7 %
$f_2 = DC\,(60)$	0.107	0.065	39.2 %

Fig. 15. Comparison of total pressure contours at the outlet plane in baseline geometry and the optimized geometries.
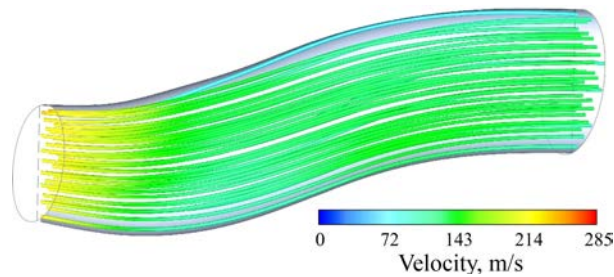
Fig. 16. Streamlines in the optimized geometry.

Fig. 17. The comparison of the cross sections of the optimized (1) and the baseline (2) geometries.
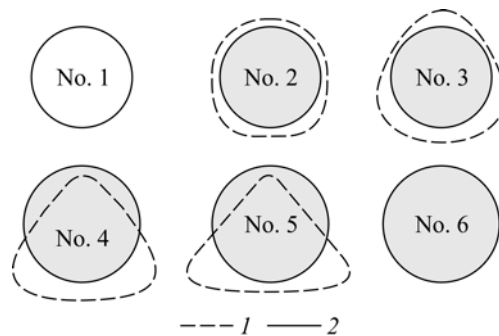

Figure 13 shows the velocity contours in the symmetry plane of the duct in the optimized and baseline geometries. As could be seen, the separation region has reduced significantly after the first bend using the egg-shape section due to the acceleration of the flow.

Figure 15 shows the total pressure loss contours at the duct outlet plane in optimized and baseline geometries. Although there is a slight non-uniformity on some parts of the duct outlet plane, the layer's thickness with low momentum has reduced distinctly at the duct outlet section. By decreasing boundary layer thickness, the useful cross section of the duct is increased. The reason for the local non-uniformities is the egg-shaped profile after the first bend. Figure 8 shows an overview of the optimized geometry, and Figure 17 shows the optimized and baseline geometry cross sections.

Conclusion

In this research, the genetic algorithm has been used for S-shaped duct optimization. To reduce calculation time, the genetic algorithm has been coupled with artificial neural networks. This optimization aimed to minimize total pressure loss and flow distortion on the duct outlet plane. Two different optimizations have been done with different design parameters. In the first optimization, the duct inlet and outlet were constant, and only the area ratio of sections and centerline *y*-coordinates of the duct have been changed. This optimization has led to improving total pressure loss and distortion by 32.5 % and 35.8 %, respectively.

In the second optimization and the area ratio of sections and centerline y-coordinates, duct section shapes have also been changed. As a result, the total pressure loss and flow distortion have been reduced by 35.7 % and 39.2 %, respectively.

Nomenclature

A — area, m^2,
C_p — total pressure coefficient,
DC — distortion coefficient,
M — Mach number,

P — pressure, Pa,
PR — pressure recovery,
r — radius, m.

Greek symbols

θ — angle, degree.

Subscript

0 — total conditions,
cl — centerline,

in — inlet,
out — outlet.

Reference

1. **M. Saneinejad and M. Nili-Ahmadabadi,** Investigating the performance of classical methods for improving flow quality inside an S-shape air inlet using numerical solution, 6th Iranian Aerospace Society Conference, 2006.
2. **S. Wellborn, B. Relichert, and T. Okiishi,** An experimental investigation of the flow in a diffusing S-duct, 28th Joint Propulsion Conf. and Exhibit, 1992, AIAA Paper, No. P. 92-3622.
3. **Q. Xiao and M.H. Tsai,** Computation of transonic diffuser flows by a lagged *k-ω* turbulence model, J. Propulsion and Power, 2003, Vol. 19, P. 473–483.
4. **G.A. Gerolymos, S. Joly, M. Malle, and I. Vallet,** Reynolds-stress model flow prediction in aircraft engine intake double-S-shaped duct, J. Aircraft, 2010, Vol. 47, P. 1368–1381.
5. **B.J. Lee and C. Kim,** Automated design methodology of turbulent internal flow using discrete adjoint formulation, Aerospace Sci. and Technology, 2007, Vol. 11, Iss. 2–3, P. 163–173.
6. **C. Fiola and R.K. Agarwal,** Simulation of secondary and separated flow in a diffusing S-duct, 52nd Aerospace Sci. Meeting, 2014, AIAA Paper, No. 2014–0561.
7. **E. Manca,** Unsteady aerodynamic investigation of the flow within an optimized S-duct intake, MSc Thesis, Cranfield University, Cranfield, 2016.
8. **S. Ghosh, D. Pratihar, K. Maiti, and P.K. Das,** An evolutionary optimization of diffuser shapes based on CFD simulations, Inter. J. Numer. Meth. Fluids, 2010, Vol. 63, P. 1147–1166.
9. **F. Furlan, N. Chiereghin, T. Kipouros, E. Benini, and M. Savill,** Computational design of S-duct intakes for distributed propulsion, Aircraft Engng Aerospace Technology, Inter. J., 2014, Vol. 86, Iss. 6, P. 473–477.
10. **A. Rigobello,** A multi-objective shape optimization of an S-duct intake through NSGA-II genetic algorithm, MSc Thesis, Padova University, Padova, 2016.
11. **L. Zeng, D. Pan, and S. Ye,** A fast multi-objective optimization approach to S-duct scoop inlets design with both inflow and outflow, Proc. Inst. Mechanical Engineers. Part G, J. Aerosp. Engng, 2018, Vol. 233, P. 3381–3394.
12. **A. Madadi, M. Kermani, and M. Nili-Ahmadabadi,** Aerodynamic design of S-shaped diffusers using ball–spine inverse design method, J. Engng for Gas Turbines and Power, 2014, Vol. 136, Iss. 12, P. 122606-1–122606-8.
13. **N. Chiereghin, L. Guglielmi, A.M. Savill, T. Kipouros, E. Manca, A. Rigobello, M. Barison, and E. Benini,** Shape optimization of a curved duct with free form deformations, in 23rd AIAA Computational Fluid Dynamics Conf., 2017, P. 4114.
14. **E. Immonen,** Shape optimization of annular S-ducts by CFD and high-order polynomial response surfaces, Engng Computations, 2018, Vol. 35, Iss. 2, P. 932–954.
15. **W. Gan and X. Zhang,** Design optimization of a three-dimensional diffusing S-duct using a modified SST turbulent model, Aerospace Sci. and Technology, 2017, Vol. 63, P. 63–72.
16. **S. Sadatpour and A. Madadi,** Optimization of S-shaped inlet diffuser; improvement of total pressure loss and flow uniformity, Amirkabir J. Mechanical Engng, 2019, Vol. 52, Iss. 11, P. 2.
17. **J. Seddon and E.L. Goldsmith,** Intake aerodynamics: an account of the mechanics of flow in and around the air intakes of turbine-engined and ramjet aircraft and missiles, Collins, London, 1985.